Distribution of the color fields around static quarks: Flux tube profiles

Richard W. Haymaker, Vandana Singh, and Yingcai Peng
Department of Physics and Astronomy, Louisiana State University, Baton Rouge, Louisiana 70803-4001

Jacek Wosiek
*Institute of Physics, Jagellonian University, Reymonta 4 Cracow, Poland**
and Max-Planck-Institut für Physik–Werner-Heisenberg-Institute, P.O. Box 40 12 12, D-85740 Munich, Germany
(Received 1 July 1994)

We report detailed calculations of the profiles of energy and action densities in the quark-antiquark string in SU(2) lattice gauge theory. We conclude that at a q-$\bar{q}$ separation $R \approx 1.0$ fm we are beginning to see the asymptotic flux tube. By employing the Michael sum rules we further conclude that the peak energy density approaches a constant in R.

PACS number(s): 11.15.Ha, 12.38.Gc

I. INTRODUCTION

Although gross features of the string connecting a quark and an antiquark are understood, little is known about the detailed structure of the flux tube. Questions remain as to the size and shape of the energy distribution. The linearly rising potential can be understood if the energy per unit length of the string is independent of the separation of the quark and antiquark. That still allows for a variation of the peak density and the width. We are also interested in the fields themselves; for example, whether they are governed by dual superconductivity, whether they appear Coulomb-like at small separations as expected from asymptotic freedom, and what excited strings look like.

Building on earlier work by a number of authors [1–12], this paper addresses the issue of the energy distribution at zero temperature. The difficulties of getting good signal-to-noise measurements at large $q\bar{q}$ separations are well known. There are tradeoffs in every strategy. Our choice is to represent the $q\bar{q}$ sources via a Wilson loop enhanced using the Parisi, Petronzio, and Rapuano [13] noise reduction techniques. Trottier and Woloshyn [14] chose this route in a recent flux calculation in three dimensions. We then attempt to extrapolate our results to large time extent of the loops. Alternative smearing techniques have been developed to increase the overlap with the ground state. This has been applied to many problems and an early review is given by Marinari [15]. In a recent conference proceedings Bali, Schlichter, and Schilling [16] have applied these techniques to the present flux problem. Another alternative is to use Polyakov lines to represent the sources. But then the "area law" forces one to work at finite temperature and then extrapolate to zero temperature.

There have been some analytical predictions of flux tube properties. Lüscher, Munster, and Weisz have studied the bosonic string model of the effective tube [17,18]. Their results show that the flux tube width has a logarithmic behavior with the quark separation R. Adler constructed a dielectric model [19], which predicts that the energy peak density in the flux tube $\sim 1/R$, and the flux tube width $\sim \sqrt{R}$. Baker, Ball, and Zachariasen have obtained the flux tube solution for QCD from the dual formulation of the Yang-Mills theory. They give analytical evidence for flux tube formation in QCD [20].

In this paper we report detailed calculations of the spacial profiles of energy and action distributions of the flux tube. This is a companion paper to Ref. [9]. Preliminary results of the present work were reported in the QCD vacuum structure conference proceedings [12]. In Ref. [9] we developed techniques to extrapolate flux measurements to infinite time extent of the Wilson loops. The transfer matrix eigenvalues were determined from the Wilson loops. We tested the global Michael sum rules [21]. We also included in that work a study of the energy and action on the midplane between the $q\bar{q}$ pair. However, it was only the integrated flux over the whole plane that was needed there. In the present paper we have redone the analysis of the same data in a way to extract profiles of the flux tube using the transfer matrix eigenvalues determined in the earlier work. Section II pulls together some of the simulation details for completeness.

There are six orientations of plaquettes corresponding to the six components of chromoelectric and chromomagnetic fields. We assign the plaquette value to the field squared at the center of the plaquette. Hence all components are defined at different space-time points. Interpolation in four dimensions is required in order to add these functions to come up with the energy density. We decided on a method used widely in other fields termed "Kriging." Applied to a regular lattice, it gives a prescription to assign weights to nearest neighbors, next-to-nearest neighbors, etc. It adapted nicely to four dimensions without biasing any particular direction in four-space. This is described in Sec. III. In this way we can fill in values

*Permanent address.

at every point on a lattice with lattice constant $a/2$ and then all components are compatible.

Also in this section we discuss the parametrization of the flux tube profile on the plane perpendicular to the line joining the quark and antiquark at the midpoint between them. It is very difficult to get accurate moments of these profiles since they are dominated by values of the flux at large transverse distance where data are very scant. Our compromise was to find a good fitting function with a very economical parametrization. We settled on a simple function that is exponential for large distance and Gaussian for small distances. It did remarkably well in that the fit was very insensitive to the sample of points used to fit over a very wide range of transverse distances.

Having determined the profile parameters for a wide range of Wilson loops, we then extrapolate these parameters to large time extent of the Wilson loops. In Sec. IV we carry out this extrapolation and present results.

II. SIMULATION

The lattice observable needed to measure the flux is [1–5]

$$f^{\mu\nu}(x) = \frac{\beta}{a^4}\left(\frac{\langle W P_x^{\mu\nu}\rangle}{\langle W\rangle} - \langle P\rangle\right) ,$$

$$\approx \frac{\beta}{a^4}\left(\frac{\langle P_x^{\mu\nu} - W P_{x_R}^{\mu\nu}\rangle}{\langle W\rangle}\right) , \qquad (1)$$

where W is the Wilson loop, $P_x^{\mu\nu}$ the plaquette located at x, $\beta = 4/g^2$, and x_R is a distant reference point. In the classical continuum limit

$$f^{\mu\nu} \overset{a\to 0}{\longrightarrow} -\frac{1}{2}\langle (F^{\mu\nu})^2\rangle_{q\bar{q}\ \mathrm{vac}} , \qquad (2)$$

where the notation $\langle\cdots\rangle_{q\bar{q}\ \mathrm{vac}}$ means the difference of the average values in the $q\bar{q}$ and vacuum state. From now on we shall be using field components in Minkowski space notation, hence

$$f^{\mu\nu} \to \frac{1}{2}(-B_1^2, -B_2^2, -B_3^2; E_1^2, E_2^2, E_3^2) . \qquad (3)$$

Correspondence between various components and $f^{\mu\nu}$ is standard: space-space plaquettes are magnetic, space-time plaquettes are electric. The energy and action densities are, respectively,

$$\epsilon = \frac{1}{2}(E^2 + B^2) ,$$

$$\gamma = \frac{1}{2}(E^2 - B^2) . \qquad (4)$$

Since the magnetic contribution turns out to be negative, there is a strong cancellation between the two terms in the energy, whereas they are enhanced in the action. One remark is that the measured negative magnetic energy density B^2 was obtained from the difference between the value of the $q\bar{q}$ state and that of the vacuum, as shown in Eq. (2). To understand the physical origin of the negative B^2, one needs to study the dynamical properties of SU(N) vacuum, which has not been fully understood.

In the earlier paper [9], we gave some of the details of the simulation and measurement techniques. Briefly, our lattice size is $17^3 \times 20$. We ran three values of $\beta = 2.3$, 2.4, and 2.5. The corresponding lattice spacings $a(\beta)$ were taken to be $a(2.3) = 0.171$ fm, $a(2.4) = 0.128$ fm, and $a(2.5) = 0.089$ fm. We measured Wilson loops for all sizes up to 7×9 which are reported in Ref. [9] as well as the eigenvalues of the transfer matrix calculated from these loops.

An important ingredient in our simulation is the analytic multihit technique in which one evaluates link integrals of the operators being measured. When this is applied to a single link on a Wilson loop the result can be given in closed form:

$$\int [dU] U \exp\left(\frac{\beta}{2}\,\mathrm{tr}[UK^\dagger]\right)$$

$$= \frac{I_2(\beta b)}{I_1(\beta b)} V \int [dU] \exp\left(\frac{\beta}{2}\,\mathrm{tr}[UK^\dagger]\right) , \qquad (5)$$

where K is the sum of six "staples" coupling to given U in the action [13], and $I_n(x)$ is the modified Bessel function. The sum of SU(2) matrices in the $j = \frac{1}{2}$ representation is a multiple of an SU(2) matrix which we denote by V:

$$K = bV, \quad b \equiv (\det K)^{1/2} . \qquad (6)$$

Effectively, what has happened is that the link has been replaced by a sum of staples associated with that link times a gauge invariant weight given by the ratio of modified Bessel functions.

Figure 1 shows the links involved. The original links in the Wilson loop and plaquette are the bold lines. The staple links are also shown. It is clear from this picture

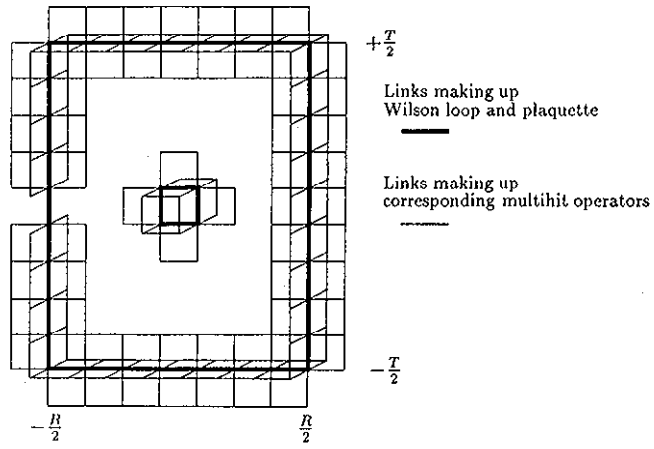

FIG. 1. Links involved in link, corner, and plaquette integrals.

that not all the links on the Wilson loop can be evaluated with Eq. (5). The criterion to be able to use Eq. (5) to evaluate a particular (bold) link is that the corresponding staples do not involve any of the other bold links. A straight line of links satisfies this criterion, but links forming a corner do not. Therefore the plaquette and the corners of the Wilson loop have to be treated separately. Further, since we are trying to measure the self-energy of the quarks we need to bring the plaquette close to and, in fact, touching the Wilson loop which will result in further special cases. It is expedient to measure the Wilson loop and plaquette for each position and orientation independently and then evaluate the cross correlation. This is fine as long as a bold link on the Wilson loop does not overlap with a staple link on the multihit plaquette or vice versa. Since we make use of fast Fourier transforms to do the cross correlations, all relative positions of the two are automatically obtained. We must then go back and recalculate the correct exceptions separately. We have the choice of either doing more integrals analytically or drop back to fewer analytic integrations for these exceptions. We chose the latter, maintaining all possible analytic integrations that could be constructed with the above three analytic results. Working in three dimensions, Trottier and Woloshyn [14] use the single link integrations and an iteration of them due to Mawhinney [22] where the above conflicts do not arise rather than employing the corner or plaquette integral.

Our compromise in all these special cases was the following: We calculated (a) the plaquette and multihit plaquette, and (b) the Wilson loop with all multihit links and the Wilson loop with a gap as shown in Fig. 1. Then the correlations were done using three cases: (i) for large separations of the Wilson loop and plaquette, all links were multihit; (ii) as the plaquette is brought close to the Wilson loop, the multihit plaquette was dropped; and (iii) when the plaquette was brought in contact with the Wilson loop, certain multihit links were also dropped as indicated by the gap in Fig. 1. This compromise means that having chosen the gap in one particular direction we cannot get self-energy data at other places on the loop, for example, to explore the self-energy for a loop with T and R reversed.

The plaquette and corner integrals cannot be done in closed form but can be evaluated using a character expansion. Details can be found in the appendix of Ref. [6]. This was based in large part on Ref. [23]. For completeness we would like to pull together just the results.

A. Character expansions

The basic technique used here is to expand the integrands using group characters as basis functions. The character is given by the trace of the $(2j+1)$-dimensional rotation matrices:

$$\chi^{(j)}(U) = \sum_m D^{(j)}_{mm}(U) = \frac{\sin[(2j+1)\psi]}{\sin\psi}, \qquad j = 0, \frac{1}{2}, 1, \frac{3}{2}, \ldots . \quad (7)$$

We parametrize group elements by an axis of rotation $\hat{n}$ and an angle of rotation about that axis denoted here by 2ψ:

$$U = \cos(\psi) + i\,\sin(\psi)\hat{n}\cdot\vec{\tau}\ , \quad (8)$$

and the group manifold is then the hypersurface of the sphere in four dimensions, S_3, and the invariant group integration measure is uniform on this manifold.

We will use the character expansion of a link or product of links in the action

$$e^{(\beta/2)\mathrm{tr}(U)} = \sum_j c_j(\beta)\chi^{(j)}(U),$$

$$c_j(\beta) = (4j+2)\frac{I_{2j+1}(\beta)}{\beta}\ , \quad (9)$$

where $I_{2j+1}(\beta)$ is the modified Bessel function. The sum is over all representations as indicated in Eq. (7). All integrations can be done making use of the orthogonality of the group integration:

$$\int [DU] D^{(j)}_{mn}(U)^* D^{(j')}_{m'n'}(U) = \frac{2\pi^2}{2j+1}\delta_{jj'}\delta_{mm'}\delta_{nn'}\ . \quad (10)$$

From this relation we can find, for example,

$$\int [dU]\chi^{(j)}(VU)\chi^{(j')}(U) = \frac{2\pi^2}{2j+1}\delta_{jj'}\chi^{(j)}(V)\ , \quad (11)$$

where V is also a link or product of links. This formula is very useful in evaluating the following integrals.

B. Corner integral

Consider the integral over two links that form a corner:

$$\langle U_2 U_1\rangle \equiv \frac{1}{Z}\int [dU_1 dU_2] U_2 U_1 e^{-S}\ ,$$

$$Z \equiv \int [dU_1 dU_2] e^{-S}\ , \quad (12)$$

where the relevant terms in the action are

$$-S \equiv \frac{\beta}{2}[\,\mathrm{tr}(W^\dagger U_2 U_1) + b_1\mathrm{tr}(U_1 V_1^\dagger) + b_2\mathrm{tr}(U_2 V_2^\dagger)]\ . \quad (13)$$

This equation defines W; b and V are defined in Eqs. (5) and (6). Z can be evaluated immediately using Eq. (11):

$$Z = \sum_j \frac{(2\pi^2)^2}{(2j+1)^2} c_j(\beta) c_j(\beta b_1) c_j(\beta b_2)\chi^{(j)}(P)\ , \quad (14)$$

where

$$P \equiv W^\dagger V_2 V_1\ . \quad (15)$$

Applying the character expansion to the three terms in the action we give the final result

$$\langle U_2 U_1 \rangle = \frac{1}{Z} \sum_j \frac{(2\pi^2)^2}{(2j+1)^2} c_j(\beta b_1) c_j(\beta b_2)$$

$$\times \left(W c_j' \chi^{(j)}(P) + c_j(\beta) \frac{[V_2 V_1 - W \frac{1}{2} \chi^{(1/2)}(P)][(j+1)\chi^{(j-1/2)}(P) - j\chi^{(j+1/2)}(P)]}{\beta(1 - \frac{1}{4}\chi^{(1/2)}(P)^2)} \right) , \quad (16)$$

where $c_j' = dc_j(\beta)/d\beta$.

C. Plaquette integral

In the plaquette integral, at most one link can be evaluated with Eq. (5). Further, it is clear that only two of the links forming a corner can make use of Eq. (16). Since the plaquette is now a gauge-invariant trace of four links, this case is in fact considerably simpler than the corner integral. Again the details can be found in Ref. [6]. Consider the four-link integral

$$Z(\gamma, \beta) \equiv \int [dU_1 dU_2 dU_3 dU_4] e^{-S} , \quad (17)$$

where

$$-S \equiv \left(\frac{\gamma}{2} \mathrm{tr}[U_4^\dagger U_3^\dagger U_2 U_1] + \frac{\beta}{2} \sum_{k=1}^{4} \mathrm{tr}[U_k K_k^\dagger] \right) . \quad (18)$$

We have displayed explicitly the dependence of the action on the links making up a particular plaquette. Each K_k matrix is the sum of *five* staples. The results are

$$Z(\gamma, \beta) = \sum_j c_j(\gamma) \frac{(2\pi^2)^4}{(2j+1)^4}$$

$$\times \prod_{k=1}^{4} c_j(\beta b_j) \chi^{(j)}(V_4^\dagger V_3^\dagger V_2 V_1) . \quad (19)$$

Pulling this together, we get the result

$$\int \left[\prod_l dU_l \right] \frac{1}{2} \mathrm{tr}(U_4^\dagger U_3^\dagger U_2 U_1) e^{-S}$$

$$= \frac{[\partial Z(\gamma, \beta)/\partial \gamma]|_{\gamma=\beta}}{Z(\beta, \beta)} \int \left[\prod_l dU_l \right] e^{-S} . \quad (20)$$

Using the plaquette and corner integrals one can reduce statistical fluctuations in the simulations significantly, because the measured values of plaquette and corner of Wilson loop involve many more links.

III. DATA INTERPOLATION AND FITTING

The goal of this work is to bring all the data on finite $T \times R$ sources into an economical parametrization so that it is comprehensible and one can easily see the trends. Two issues arise: (i) interpolation of six plaquette orientations since they are all defined at different space-time points, and (ii) guided by the data itself, find a "best" parametrization.

A. Interpolation

The six components of the flux $f^{\mu\nu}(x)$ are defined at the center of the corresponding plaquette and hence are all at different space-time points. To get information on the flux tube we need the best possible estimate of all components on the transverse plane defined at the center of the Wilson loop for both even and odd T and even and odd R. This leads to a rather complex pattern of neighbors and nearest neighbors. Getting plaquettes with six orientations to agree among themselves where best to talk to each other under these circumstances is not as simple as it sounds. In order to combine them we employed a four-dimensional interpolation method that minimizes the variance of the estimated value of the function. In other words, as one varies the value of each input point over, say, one standard deviation, one requires that the linear interpolated function be as insensitive as possible. There is much literature on this under the name of Kriging [24] in mining engineering and a two-dimensional version is employed in surface plot software.

Consider a function $f(x)$ that is given as a statistical variable at a set of points x_j. Suppose the mean $\langle f(x) \rangle$ and variance $\sigma_{x_j}^2 = \langle (f(x_j) - \langle f(x_j) \rangle)^2 \rangle$ are known. Define an estimate of the function, $\tilde{f}(x)$, as the linear combination

$$\tilde{f}(x) = \sum_j a_j f(x_j) , \quad (21)$$

where the sum is over a subset of the points, and the coefficients a_j's are functions of the set of points $\{x_j\}$ and the point x. Now use this estimate to evaluate the function at one of the given points x_i and consider the

variance of the difference of the function $f(x_i)$ and its estimate $\tilde{f}(x_i)$:

$$\sigma_e^2 = \langle [(f(x_i) - \langle f(x_i)\rangle) - (\tilde{f}(x_i) - \langle \tilde{f}(x_i)\rangle)]^2\rangle = \sigma_{x_i}^2 - 2\sum_j a_j \sigma_{x_i,x_j}^2 + \sum_{jj'} a_j a_{j'} \sigma_{x_j,x_{j'}}^2 \ . \quad (22)$$

The sum excludes the point x_i. The covariance matrix is defined

$$\sigma_{x_k,x_l}^2 = \langle (f(x_k) - \langle f(x_k)\rangle)(f(x_l) - \langle f(x_l)\rangle)\rangle \ . \quad (23)$$

The Kriging method determines the coefficients a_j by minimizing σ_e^2 subject to a constraint; i.e., we minimize

$$\mathcal{L}(a_j) = \sigma_e^2(a_j) + 2\mu \left(\sum_j a_j - 1 \right) \ , \quad (24)$$

where μ is a Lagrange multiplier. The constraint arises from the condition that when applied to all points in the set, $\tilde{f}(x_i)$ underestimates $f(x_i)$ as often as it overestimates it:

$$\left\langle\!\!\left\langle \sum_j a_j f(x_j) - f(x_i) \right\rangle\!\!\right\rangle = 0 \ . \quad (25)$$

Using $\langle\!\langle f(x_i)\rangle\!\rangle = f$ gives the constraint $\sum_j a_j = 1$. Hence the coefficients are given by the equations

$$\sum_{j'} \sigma_{x_j,x_{j'}}^2 a_{j'} + \mu = \sigma_{x_i,x_j}^2 \ ,$$

$$\sum_{j'} a_{j'} = 1 \ . \quad (26)$$

We want to apply this to interpolate $f(x)$ at a general point. The a_j's are determined from the covariance matrix at the general point. Since the a_j's are independent of the overall normalization of the covariance matrix and the relevant property is how the covariance matrix varies with distance between the two arguments, so in practical applications one assumes that the covariance matrix falls as a function of distance, going to zero at large separations.

Our choice is

$$\sigma_{x_j,x_{j'}}^2 \sim \exp(-|j - j'|/\tau) \ . \quad (27)$$

One can easily check that if one chose the set $\{x_j\}$ to include the point x_i, then the corresponding $a_i = 1$, and all other a_j's equal zero. For a point near one of the x_j, the corresponding $a_j = 1$ dominates. Since we have an *ad hoc* ansatz for the covariance matrix, the actual errors in our data do not enter in the interpolation. In fact this is just a method of linear interpolation which weighs the nearby points more than the far points which is divorced from its statistical origins.

The freedom in this method is in the choice of neighboring points and the value of the correlation length τ. Our criterion was to keep the correlation parameter τ as small as possible while at the same time interpolating in a way that did not introduce obvious irregularities of the order of a lattice spacing on accurate data sets with minimal fluctuation. We found $\tau \sim$ the lattice spacing and a radius that included one or two dozen points in the four-dimensional neighborhood of the interpolated point. The errors were calculated by linearly interpolating the errors from the neighboring points. This overestimates the errors since it assumes that the values used to interpolate are completely correlated. Assuming they are completely uncorrelated, and then interpolating the variance gives an error typically less than half of the linearly interpolated errors. Since we do not know the covariance matrix we took the worst case.

Using this method we filled in every point at the half lattice spacing for each component which then allowed us to combine any components. Figures 2 and 3 give surface plots of the interpolated data for a Wilson loop of $T = 7$ and $R = 5$ with $\beta = 2.4$. Shown are two sections, one through the two quarks and the second on a plane midway between the two quarks to show the flux tube profile. Errors tend to be fairly constant for a particular $R \times T$ data set. Ripples in the background indicate the size of the scatter.

Figure 2 shows the electric and magnetic components $\frac{1}{2}E_{\parallel}^2$, $-\frac{1}{2}B_{\parallel}^2$, $\frac{1}{2}E_{\perp}^2$, and $-\frac{1}{2}B_{\perp}^2$. From these plots we can see that only the electric components have prominent peaks around the quarks, and the two transverse components, $\frac{1}{2}E_{\perp}^2$ and $-\frac{1}{2}B_{\perp}^2$, are essentially the same. These two components cancel in calculating the energy and add in the action. They are the widest of the four profiles and hence the action has a wider profile than the energy. The "shoulder" in Fig. 2(a) is an artifact that remains after tuning the interpolation parameters for the best overall performance. This artifact is not apparent when all six components are combined in the pictures that follow.

Figure 3 shows the action and energy for the same parameters as above. The peaks around the quarks rise above the background equally in the energy and action since they come predominantly from the electric components. The Michael sum rules confirm this behavior as described in the earlier paper [9]. The flux tube profiles for action and energy are quite different. Note the large cancellation in the energy compared to the action and the resulting difficulty in measuring the former. Rotational symmetry is reasonably well restored in the action profiles, but there are large lattice artifacts in the energy profiles.

B. Fit to profile function

The basic parameters we are interested in are the peak value and widths of the flux density of the energy and action. Obtaining good data on the second moment of the profile in order to determine its width is problematic. The profiles fall sharply and the fourth moment needed

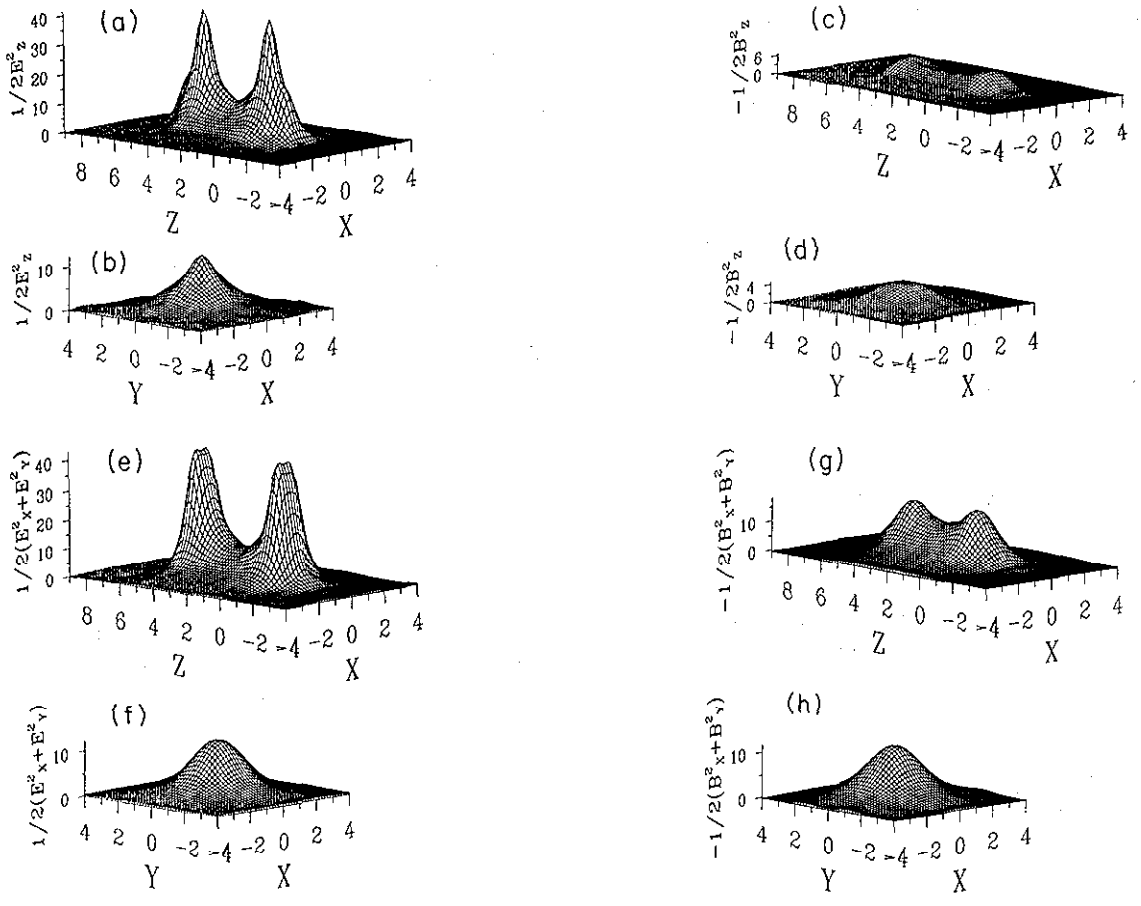

FIG. 2. Surface plots of electric and magnetic components. For each component two sections are shown, one is on the longitudinal plane containing the $q\bar{q}$ pair, another is on the transverse plane midway between the $q\bar{q}$ pair, (a) and (b) are for $\frac{1}{2}E_{\parallel}^2$, (c) and (d) for $\frac{1}{2}B_{\parallel}^2$, (e) and (f) for $\frac{1}{2}E_{\perp}^2$, (g) and (h) for $-\frac{1}{2}B_{\perp}^2$. The data were measured on the Wilson loop with $T = 7$, $R = 5$, and $\beta = 2.4$.

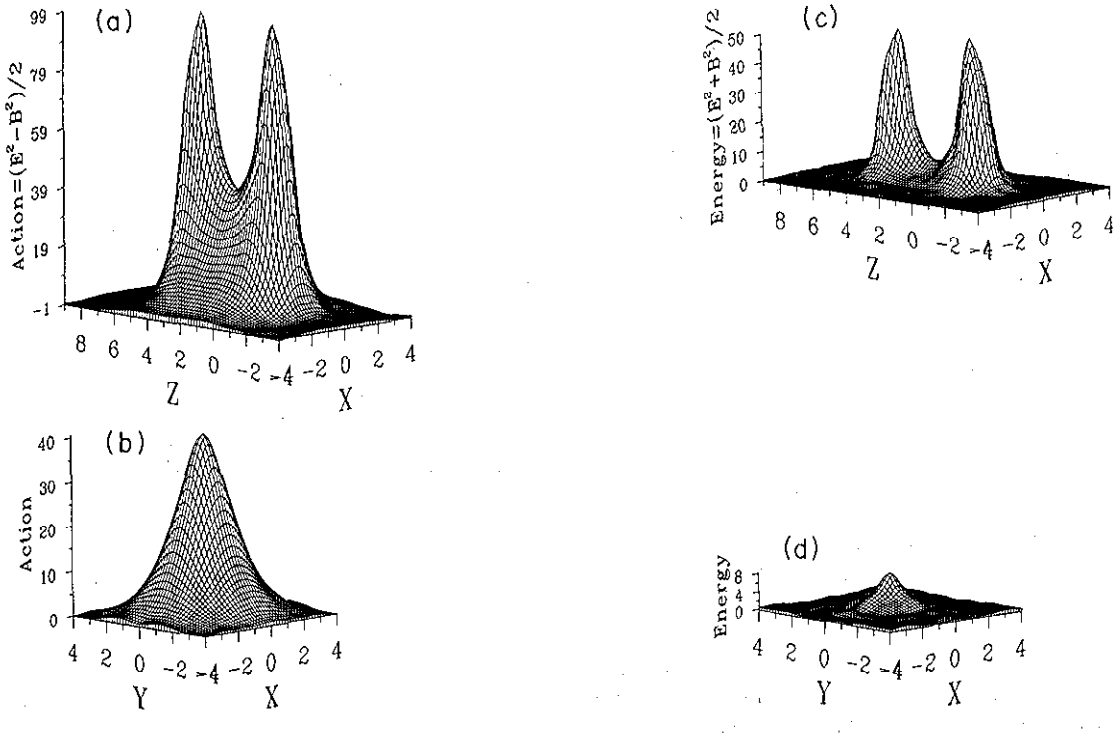

FIG. 3. Surface plots of energy and action, similar to Fig. 2, and obtained from the same data set. (a) and (b) are for the action density, (c) and (d) for the energy density.

TABLE I. The fitting parameters for the action distributions with $\beta = 2.3$ and various Wilson loop sizes, T and R. For each loop size we list in order the values of the three parameters, A in GeV/fm^3, B in fm, and D in fm. The last value in each case gives the integration of the area under the curve in GeV/fm. This table can be filled in by using the $R \leftrightarrow T$ symmetry.

R \ T	3	4	5	6	7	8
3	53.0(1)	47.9(1)	44.9(2)	43.4(3)	42.1(5)	40.4(9)
	0.1328(2)	0.1495(4)	0.1597(6)	0.167(1)	0.172(2)	0.176(4)
	0.1041(2)	0.1105(3)	0.1175(6)	0.121(1)	0.130(2)	0.136(4)
	6.58(3)	7.21(5)	7.69(8)	8.05(14)	8.4(3)	8.6(5)
4		41.7(1)	38.6(2)	37.7(5)	36.0(10)	34.0(10)
		0.1729(5)	0.189(1)	0.196(3)	0.198(5)	0.198(8)
		0.1177(4)	0.123(1)	0.135(2)	0.149(5)	0.153(9)
		7.95(6)	8.55(14)	9.2(3)	9.7(6)	9.0(10)
5			34.5(3)	34.6(7)	35.0(10)	42.0(30)
			0.210(3)	0.213(5)	0.23(1)	0.20(2)
			0.107(1)	0.128(3)	0.17(1)	0.16(2)
			8.5(2)	9.3(6)	12.0(20)	12.0(30)
6				31.0(10)	39.0(40)	
				0.22(1)	0.19(2)	
				0.058(3)	0.036(4)	
				6.7(8)	7.0(10)	

TABLE II. The fitting parameters for the energy distributions with $\beta = 2.3$ and various Wilson loop sizes, T and R. Further definitions are given in Table I. This table is not symmetric in R and T; the violations measure the transverse component contribution to the energy.

R \ T	3	4	5	6	7	8
3	24.1(1)	18.4(1)	16.0(2)	14.1(4)	13.8(6)	13.0(10)
	0.0813(4)	0.0897(8)	0.0925(15)	0.091(4)	0.096(5)	0.093(9)
	0.0787(5)	0.0817(9)	0.0878(18)	0.092(4)	0.085(6)	0.088(10)
	1.33(2)	1.17(3)	1.13(5)	1.02(10)	0.98(14)	0.92(22)
4	17.7(1)	13.2(2)	10.4(3)	9.0(6)	8.0(10)	7.0(10)
	0.094(1)	0.104(1)	0.109(4)	0.115(9)	0.12(2)	0.12(1)
	0.088(1)	0.093(2)	0.115(6)	0.112(12)	0.10(2)	0.020(2)
	1.28(3)	1.12(4)	1.13(11)	1.0(2)	0.8(4)	0.47(14)
5	15.6(2)	10.8(4)	7.8(4)	6.0(20)	3.0(10)	
	0.0924(17)	0.105(4)	0.12(1)	0.14(7)	0.20(5)	
	0.097(2)	0.102(5)	0.16(3)		0.024(6)	
	1.21(6)	0.99(11)	1.3(3)			
6	13.2(4)	9.0(6)	6.0(10)	5.0(20)		
	0.100(4)	0.118(9)	0.13(3)	0.2(1)		
	0.106(5)	0.099(6)	0.11(3)	0.04(2)		
	1.21(12)	0.93(18)				
7	12.3(7)	8.2(40)	4.0(20)			
	0.095(8)	0.12(2)	0.10(3)			
	0.115(14)	0.14(5)	0.14(8)			
	1.16(23)	1.2(6)				
8	10.5(8)	8.0(10)				
	0.098(5)	0.15(2)				
	0.137(12)	0.21(7)				
	1.2(6)					

to estimate error would be sampling only large distances from the axis where the signal-to-noise is small. Instead we fitted the energy and action density in the plane at the midpoint between q and $\bar{q}$ using the function

$$f(r_\perp) = a\exp(-\sqrt{c^2 + (r_\perp/b)^2}) \tag{28}$$

or rewriting, in terms of the width at half maximum, B,

$$f(r_\perp) = Ae^C \exp[-\sqrt{C^2 + (2C\ln 2 + \ln^2 2)(r_\perp/B)^2}]\,. \tag{29}$$

The peak value A and the width B are determined for each of 70 cases of different loop sizes and values of β. (We used Minuit to determine the fit and errors.) For the third parameter we chose the decay length of the tail of this function, $D = B/\sqrt{(2C\ln 2 + \ln^2 2)}$. This parameter was less well determined. We attempted to include an additive constant to the function since our sum rule paper gave evidence for it. However this gave too much freedom to the fit and gave unstable answers. We also tried a Gaussian plus background constant and this did not fit nearly as well as the function chosen. In conclusion, the data are not good enough to determine four parameters. There is still some ambiguity as to how to assign parameters to this form. But we found the peak value A and width at half maximum B are well determined. The exponential falloff of this function is more difficult to pin down. It perhaps is modeling a true exponential falloff plus possibly a background which we believe is there due to the fact that we are measuring the flux relative to a reference point that is not at infinity.

The modeling of these data with a χ^2 criterion is not applicable because the fitting functions cannot fit the azimuthal irregularities arising from the cubic symmetry. This is pronounced for small R and T where the error bars are quite small. We must keep the number of parameters small in order to be able to make predictions and modeling this breaking of axial symmetry is not viable. We did a least-squares fit to average out these angular irregularities. Technically it was essentially the same as a χ^2 fit since the errors are almost constant across the profile giving equal weight to all points. However, χ^2 is not a quality criterion and we must find a new one which is applicable. Minuit was used to determine the parameters and the output covariance matrix. We did not have input off-diagonal covariance matrix elements at our disposal because of the limitations in data handling of the Monte Carlo.

We tested the quality of the fit by fitting to subsets of the input points and looking for a drift in the parameters. We believe the fit is modeling the data well because of the stability of the numbers over changing the set of points used in the fit. We tried many functional forms as indicated above and the form we settled on had drift in

TABLE III. The fitting parameters for the action distributions with $\beta = 2.4$ and various Wilson loop sizes, T and R. Further definitions are given in Table I.

R \ T	3	4	5	6	7	8	9
3	103.3(1)	87.6(1)	77.7(2)	72.4(3)	69.7(4)	67.1(5)	65.0(10)
	0.0947(1)	0.1065(2)	0.1156(3)	0.1218(4)	0.1249(6)	0.128(1)	0.132(2)
	0.0796(1)	0.0874(2)	0.0938(3)	0.0970(4)	0.1001(6)	0.102(1)	0.098(2)
	6.87(2)	7.22(3)	7.45(4)	7.58(6)	7.68(9)	7.76(13)	7.7(3)
4		69.42(9)	58.8(1)	53.8(2)	50.3(3)	49.0(4)	49.0(10)
		0.1262(2)	0.1427(3)	0.1523(6)	0.160(1)	0.162(1)	0.165(5)
		0.0970(2)	0.1023(3)	0.1066(5)	0.104(1)	0.111(1)	0.119(5)
		7.60(3)	7.81(5)	7.99(7)	7.9(1)	8.11(17)	8.7(6)
5			4.87(2)	44.6(3)	40.8(4)	40.2(7)	41.(20)
			0.1653(6)	0.178(1)	1.187(2)	0.186(4)	0.19(1)
			0.1101(5)	0.120(1)	0.127(2)	0.151(6)	0.10(1)
			8.22(8)	8.64(15)	8.7(3)	9.2(5)	8.2(1.2)
6				39.3(4)	37.3(8)	38.0(3)	27.0(20)
				0.195(2)	0.204(5)	0.22(2)	0.28(3)
				0.121(2)	0.134(4)	0.18(3)	0.034(3)
				8.7(3)	9.1(5)	12.0(20)	9.7(1.7)
7					32.0(2)	24.0(30)	
					0.26(1)	0.23(3)	
					0.31(2)	0.27(3)	
					9.4(9)	5.7(1.5)	

the parameter values which was comparable or smaller than the scatter as one increased radius for a wide range of R and T. The scatter was comparable to the Minuit errors. We determined the parameters using nine sets of points, choosing the interior of circles of radius $1.5a$ to $5.5a$.

Our complete fitting results are shown in Tables I–VI for action and energy distributions. The four numbers for each loop size are the peak value, A in GeV/fm^3, the width at half maximum, B in fm, the exponential decay length, D in fm, and the integration of the area under the curve to give the string tension in GeV/fm. As a reminder, since we are looking at the middle time slice and looking at the midpoint of the flux tube, these parameters are measured in the x, y plane for z, t at the middle of the Wilson loop. The tables report the fits for radii $\leq 3.0a$ and $\leq 3.5a$.

Figure 4 illustrates an interesting general feature of our data. The cluster of three points for each R and T corresponds to the three quantities:

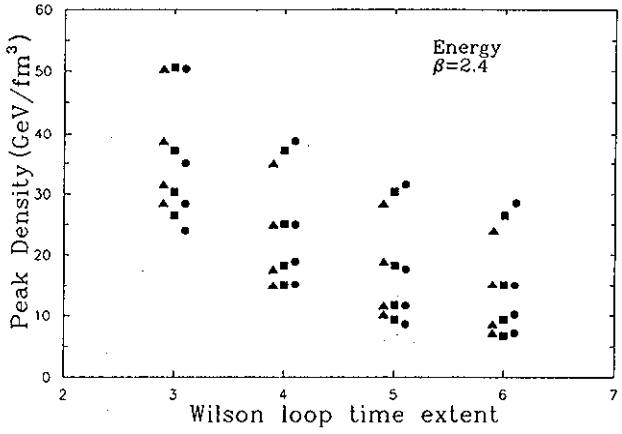

FIG. 4. Peak density for $R \times T$ Wilson loop sizes with $\beta = 2.4$ and $R = 3$–6, $T = 3$–6. For fixed T the points decrease monotonically with R. Triangles: energy density for $R \times T$ loop; circles: energy density for $T \times R$ loop; squares: $\|$ components of E^2 and B^2 only.

TABLE IV. The fitting parameters for the energy distributions with $\beta = 2.4$ and various Wilson loop sizes, T and R. Further definitions are given in Tables I and II.

R \ T	3	4	5	6	7	8	9
3	50.4(1)	38.7(2)	31.5(2)	28.5(3)	26.8(4)	25.4(6)	25.0(20)
	0.0623(2)	0.0694(3)	0.073(1)	0.073(1)	0.075(1)	0.073(2)	0.078(6)
	0.0599(2)	0.0624(3)	0.067(1)	0.069(1)	0.069(2)	0.073(3)	0.068(6)
	1.63(1)	1.47(2)	1.33(3)	1.24(4)	1.20(6)	1.17(9)	1.16(22)
4	35.0(2)	25.0(1)	17.7(2)	15.0(3)	12.9(3)	12.1(5)	12.0(20)
	0.0689(4)	0.0814(5)	0.084(1)	0.092(2)	0.094(3)	0.093(6)	0.09(2)
	0.0696(5)	0.0703(5)	0.087(2)	0.084(2)	0.090(4)	0.091(8)	0.05(1)
	1.45(2)	1.26(2)	1.12(4)	1.00(6)	0.93(7)	0.88(13)	0.6(3)
5	28.4(2)	18.8(2)	11.7(2)	10.2(4)	8.2(6)	8.1(8)	7.8(1.6)
	0.070(1)	0.084(2)	0.097(3)	0.101(6)	0.11(1)	0.100(9)	0.15(2)
	0.076(1)	0.085(2)	0.106(5)	0.108(9)	0.14(3)	0.14(3)	
	1.31(3)	1.16(4)	1.02(7)	0.94(13)	1.05(26)		0.8(3)
6	23.9(3)	15.1(3)	8.6(4)	7.2(5)	5.0(10)	5.3(1.1)	2.5(1.6)
	0.071(1)	0.095(2)	0.108(7)	0.12(1)	0.14(4)		
	0.085(2)	0.087(3)	0.117(13)	0.11(2)	0.14(8)		
	1.26(6)	1.08(6)	0.91(14)	0.8(2)	0.8(5)	3.1(1.5)	
7	22.7(3)	13.8(5)	7.3(6)	4.0(7)			
	0.070(1)	0.092(5)	0.107(13)	0.19(4)			
	0.089(2)	0.101(8)	0.13(3)	0.05(1)			
	1.23(5)	1.10(14)	0.87(25)	0.7(4)			
8	20.9(6)	12.9(7)	6.0(10)	5.0(30)			
	0.071(2)	0.096(6)	0.106(27)	0.06(3)			
	0.094(5)	0.105(11)	0.12(5)				
	1.22(9)	1.1(2)	0.7(4)				
9	22.0(20)	14.0(20)	6.0(20)	7.0(50)			
	0.074(7)	0.09(2)	0.16(6)	0.08(4)			
	0.78(11)	0.10(3)	0.06(2)	0.010(5)			
	1.09(27)	1.6(6)					

$$\epsilon = \frac{1}{2}(E_\parallel^2 + B_\parallel^2) = \frac{1}{2}(E_\perp^2 + B_\perp^2) ,$$

$$\epsilon_\parallel = \frac{1}{2}(E_\parallel^2 + B_\parallel^2) ,$$

$$\epsilon(T \leftrightarrow R) = \frac{1}{2}(E_\parallel^2 + B_\parallel^2) - \frac{1}{2}(E_\perp^2 + B_\perp^2) . \qquad (30)$$

If one turns the Wilson loop on its side, the $\parallel$ components are unchanged but the $\perp$ components of the electric and magnetic fields are reversed: $E_\perp^2 \leftrightarrow -B_\perp^2$. Hence there is a sign change in the third expression compared to the first. The central points of the cluster are the $\parallel$ components only. *The clustering of the points implies that the $\perp$ components of the electric and magnetic contributions to energy density are approximately equal but of opposite sign and cancel.* The width of the peak is even less sensitive to the transverse components giving essentially the same value for all three points.

IV. RESULTS FOR THE GROUND STATE

A. Extrapolation to infinite Wilson loop time extent

In the companion paper [9] we described the use of the transfer matrix eigenvalues to extrapolate the data to infinite time. Similar to the potential case, the finite time extent of the Wilson loop $W(R,T)$ introduces contamination of the $f^{\mu\nu}(x)$ by the excited states of the color field [7]. From the transfer matrix representation of the correlation between the Wilson loop W and a plaquette P,

$$\langle WP \rangle = Z^{-1} \mathrm{Tr}(\mathcal{T}^{L_t - T/a} S \mathcal{T}_{q\bar{q}}^{T/2a} P \mathcal{T}_{q\bar{q}}^{T/2a} S) , \qquad (31)$$

where S is the operator which excites the $q\bar{q}$ states from the vacuum, and $\mathcal{T}_{q\bar{q}}$ is the transfer matrix in the $q\bar{q}$ sector. We obtain, for any component $f^{\mu\nu}$ ($\equiv F$),

$$F = \mathcal{F} + \mathcal{R}_1 e^{-E_1 T} + \mathcal{C}_1 e^{-E_1 T/2} + \cdots \qquad (32)$$

where $\mathcal{F}$ denotes true ground state average, and E_1 stands for the energy gap of $\mathcal{T}_{q\bar{q}}$, which can be determined by fitting the Wilson loops to the exponentials as described in Ref. [9]. Formula (32) applies to any component $(\mu\nu)$ and any three-space location $\vec{x}$ of the plaquette $P^{\mu\nu}(\vec{x}, x_0)$. To minimize the effect of the cross terms, x_0 was always chosen at the middle of the time interval of the Wilson loop (hence the term $e^{-E_1 T/2}$). For any parameter extracted from the flux distribution $f^{\mu\nu}$, e.g., the peak density, one can use Eq. (32) to fit the parameter values corresponding to various Wilson loop time extents, and extract the asymptotic value $\mathcal{F}$ for $T \to \infty$.

A sample of the results of extrapolating is shown in Figs. 5, 6, and 7. We are simply trying to find the

TABLE V. The fitting parameters for the action distributions with $\beta = 2.5$ and various Wilson loop sizes, T and R, which is similar to Table I.

R \ T	3	4	5	6	7	8	9
3	301.0(10)	241.0(10)	203.0(10)	191.0(10)	178.0(20)	171.0(20)	164.0(30)
	0.0621(1)	0.0681(3)	0.0741(4)	0.0750(5)	0.0782(7)	0.079(1)	0.082(1)
	0.0511(1)	0.0574(3)	0.0626(4)	0.0682(6)	0.0699(8)	0.073(1)	0.074(2)
	8.48(5)	8.33(8)	8.3(1)	8.4(1)	8.4(2)	8.5(3)	8.5(3)
4		172.4(2)	135.2(7)	119.0(20)	110.0(10)	103.0(10)	96.0(20)
		0.0804(1)	0.0911(5)	0.0982(8)	0.103(1)	0.106(2)	0.111(3)
		0.0661(1)	0.0744(6)	0.081(1)	0.088(2)	0.093(2)	0.092(3)
		8.06(3)	8.0(1)	8.17(16)	8.4(3)	8.5(3)	8.3(4)
5			101.1(5)	85.7(7)	77.2(9)	73.0(10)	62.0(20)
			0.1111(7)	0.123(1)	0.131(2)	0.139(3)	0.148(5)
			0.0798(6)	0.085(1)	0.085(2)	0.120(5)	0.15(7)
			8.04(13)	8.0(2)	7.9(3)	9.4(5)	8.5(7)
6				71.2(8)	62.0(10)	63.0(10)	63.0(20)
				0.141(2)	0.159(3)	0.162(2)	0.177(4)
				0.078(1)	0.055(1)	0.0193(3)	0.0212(5)
				7.9(3)	7.7(5)	7.5(3)	9.0(5)
7					56.0(20)	58.0(20)	
					0.172(6)	0.158(4)	
					0.052(2)	0.0189(5)	
					7.9(8)	6.6(4)	

asymptotes of the gently decaying curves. The extrapolated values are displayed on the right (at $T = 12$). One can see for the cases $R = 3, 4, 5$ that the extrapolation looks reasonable for the height and half width. The data are deteriorating for large T for the cases of $R = 6, 7$ and even at $R = 5$ for the exponential width. Because of reasonable accuracy of the small T points, one can still make a prediction of the asymptote in some cases in spite of the large T scatter. All fits were done repeatedly exploring the effect of the dropping selected points and we report those which showed stability.

However, we found cases where another effect causes instabilities in the fit. Raw flux data commonly show decaying behavior with the points lying alternatively slightly above and below the curve in an even-odd pattern. This is particularly apparent for small T and R and is a lattice artifact. The effect is much reduced in this analysis because the parameters represent the behavior of a large number of plaquettes and we further made a special effort to interpolate well to the value at the center of the Wilson loop. But the effect is not entirely absent.

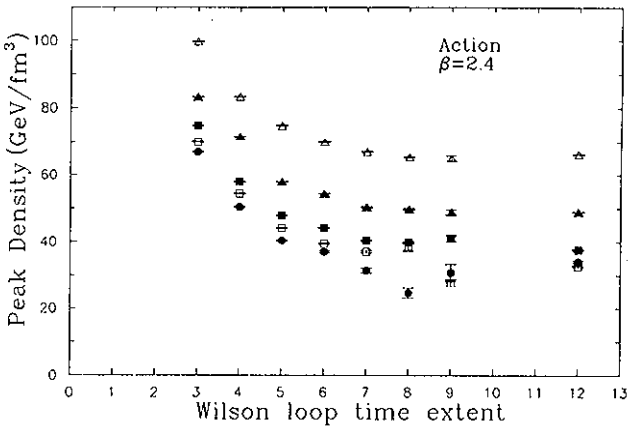

FIG. 5. Extrapolation of action peak density to infinite Wilson loop time extent. The extrapolated values are plotted at $T = 12$. The data were measured on the Wilson loop of the size $R \times T$ with $\beta = 2.4$, for $T = 3$–9 and $R = 3$ (open triangles), $R = 4$ (solid triangles), $R = 5$ (solid squares), $R = 6$ (open squares), and $R = 7$ (solid circles).

TABLE VI. The fitting parameters for the energy distributions with $\beta = 2.5$ and various Wilson loop sizes, T and R. Further definitions are given in Tables I and II.

R \ T	3	4	5	6	7	8	9
3	160.0(10)	123.0(10)	94.0(10)	85.0(10)	79.0(20)	77.0(20)	71.0(30)
	0.0437(3)	0.0487(4)	0.0517(7)	0.051(1)	0.053(1)	0.051(2)	0.055(3)
	0.0414(3)	0.0447(5)	0.048(1)	0.050(1)	0.050(2)	0.052(2)	0.051(3)
	2.50(4)	2.33(5)	2.02(7)	1.9(1)	1.8(1)	1.75(16)	1.7(2)
4	108.0(10)	75.4(6)	51.0(10)	43.0(10)	37.0(20)	33.0(20)	28.0(30)
	0.465(5)	0.0570(5)	0.059(1)	0.065(2)	0.065(4)	0.068(4)	0.072(8)
	0.484(7)	0.0488(5)	0.060(2)	0.058(2)	0.062(5)	0.060(5)	0.055(7)
	2.10(6)	1.84(4)	1.54(8)	1.4(1)	1.3(2)	1.2(2)	1.0(3)
5	82.0(10)	54.9(9)	29.2(6)	25.0(10)	17.0(10)	17.5(1.8)	16.0(20)
	0.0489(8)	0.059(1)	0.070(2)	0.071(4)	0.083(8)	0.094(13)	0.086(16)
	0.053(1)	0.062(2)	0.070(3)	0.078(8)	0.075(11)	0.052(8)	0.067(16)
	1.86(8)	1.72(9)	1.22(9)	1.16(18)	0.90(24)	0.9(3)	0.81(41)
6	71.0(10)	43.0(10)	24.0(10)	16.0(10)	8.0(20)	8.0(2.2)	6.0(1.7)
	0.048(1)	0.066(2)	0.080(5)	0.09(1)	0.12(2)	0.15(5)	0.16(3)
	0.060(3)	0.069(3)	0.088(9)	0.975(11)	0.035(7)	0.13(9)	
	1.79(12)	1.68(12)	1.4(2)	0.93(26)	0.59(28)	1.1(8)	0.7(3)
7	65.0(20)	38.0(20)	19.0(10)	14.0(20)	9.0(30)	9.0(30)	
	0.050(2)	0.066(4)	0.089(9)	0.081(16)	0.08(3)	0.11(5)	
	0.060(3)	0.071(6)	0.094(17)	0.077(22)	0.04(2)		
	1.66(15)	1.5(2)	1.3(3)	0.77(37)			
8	60.0(20)	33.9(1.5)	17.0(20)	11.0(30)	4.0(20)		
	0.048(2)	0.072(4)	0.096(14)	0.10(3)	0.21(9)		
	0.063(4)	0.067(5)	0.13(5)	0.07(3)	0.02(1)		
	1.59(15)	1.4(2)	1.6(5)				
9	55.0(30)	32.0(30)	15.0(30)	12.0(40)			
	0.051(3)	0.074(8)	0.12(3)	0.10(5)			
	0.061(6)	0.072(11)	0.14(8)				
	1.5(3)	1.4(4)	1.7(9)				

motivated us to look upon $\alpha_s^{\rm eff}$ as a process-independent quantity to confront the c and b measurements 1–7 with a unique one-parameter PT prediction.[9]

Hereafter, we fix heavy quark masses to be

$$M_c = 1.5 \text{ GeV}, \quad M_b = 4.75 \text{ GeV} . \tag{4.1}$$

(Sensitivity to the b-quark mass will be discussed below.)

A. Fitting mean quark energies

Figure 2 shows the quality of the fit to seven separate data of Table I together with the total χ^2 as a function of $\Lambda^{(5)}$ in the F model with $A = 0.191$ (the best-fit value). Some explanation is in order. In this figure (and similar plots below) for each datum the ratio

$$\frac{\text{theor} - \text{expt}}{\text{expt error}} \tag{4.2}$$

is displayed against the right vertical scale. Dashed horizontal lines mark 1σ levels for each single datum. The two curves (which should be read out against the left scale) show the squared deviation of the points (4.2) from the median, that is, the total χ^2. The solid curve sums up all seven data, while the dash-dotted one accumulates the "high W" data only. The "high W" sample we define excluding the entries No. 1 and No. 6, which correspond to the quark mass-to-energy ratios

$$M/E \approx M_c/5 \text{ GeV} \sim M_b/15 \text{ GeV} \approx \tfrac{1}{3} .$$

These two entries are subject to significant nonrelativistic corrections. The fact that the two fits are consistent is good news: It shows that the nonrelativistic effects have been properly taken into account[10] in the PT radiator (2.7).

Figure 3 demonstrates sensitivity of the PT description to the "confinement parameter." Here we have chosen the G_2 model for a change. The first thing to be noticed is that with the best-fit parameter $C_2 = 2.86$ one obtains the same value $\Lambda^{(5)} \approx 580$ MeV, a comparable quality of the fit, $\chi^2_{\rm min} \approx 0.7$, and even the same dynamics of each of seven data as in the above F-model description (Fig. 2). In the upper part of this plot, two marginal values of C_2 are also shown which correspond to one standard deviation from the total seven-fit: $\chi^2_{\rm min}(2.53) = \chi^2_{\rm min}(3.21) = \chi^2_{\rm min}(2.86) + 1$.

In Fig. 4 comparison is made of the quality of the fits within different models for the effective coupling (two loop, $n_f = 5$). For each value of Λ, the A/C parameter

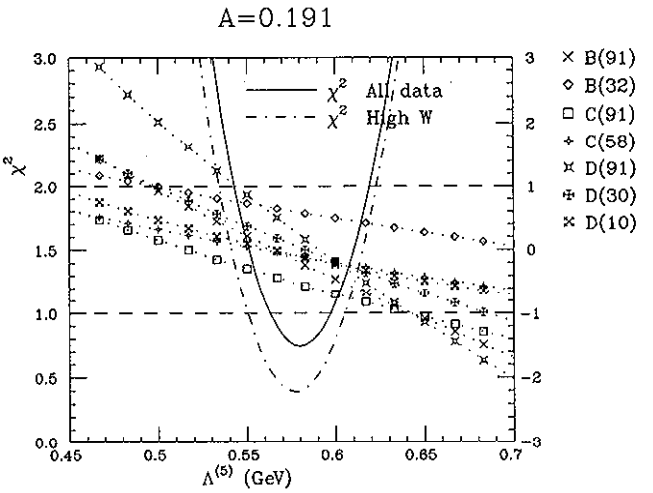

FIG. 2. Λ dependence of the F-model fit to mean energy losses (two-loop $\alpha_s^{\rm eff}$ with $n_f = 5$). The right scale shows the normalized deviation between a theoretical prediction and an experimental datum (4.2). Dashed lines mark the 1σ band. Solid and dash-dotted lines show the values of χ^2 (against the left scale) for all data and the high W data sample correspondingly.

has been adjusted to minimize the error (one-parameter fit). The upper scale shows corresponding values of $\alpha_{\overline{\rm MS}}$ at LEP recalculated from $\alpha_s^{\rm eff}$ with use of the relation (2.17b).

It is worthwhile to notice some peculiarity of the G_1 model. This model is "too soft" in a sense that it induces the *negative* preasymptotic power term $\propto k^{-2}$ in $\alpha_s^{\rm eff}(k)$, which correction suppresses $\alpha_s^{\rm eff}$ in a relatively high momentum region.

Figure 5 illustrates this peculiarity. Here the couplings corresponding to the best-fit A/C values for $\Lambda^{(5)} = 580$ MeV are compared. Solid lines $(F, G_{2\text{–}4})$ correspond to $\chi^2 \approx 0.7$. In the G_1 model shown by the dash-dotted line $(\chi^2 \approx 1.2)$, $\alpha_s^{\rm eff}$ stays noticeably smaller above 1.5 GeV before the perturbative logarithmic regime sets up and all the models merge.

As a result, to compensate for reduced radiation intensity the best-fit Λ value [and thus $\alpha(M_Z)$] within the G_1 model tends to be larger compared to "sharp" models F, $G_2, \ldots$.

Leaving G_1 aside, we conclude that both the quality of the fit and the value of Λ the "sharp" models point at hardly exhibit any model dependence. From Fig. 4 (see also Fig. 3) we deduce

$$\Lambda^{(5)} = 580 \pm 80 \text{ MeV} . \tag{4.3a}$$

Being translated into the $\overline{\rm MS}$ parameter this gives

$$\alpha_{\overline{\rm MS}}(M_Z) = 0.127 \pm 0.003 . \tag{4.3b}$$

The error here is purely statistical (one standard deviation).

[9] In spite of the fact that such a naive approach suggests the same theoretical expectation for the two physically different data No. 3 and No. 5.

[10] The relativistic version of (2.4)–(2.7) reported earlier [7] failed to properly embody the "b at 32" datum No. 6.

we can rule out a Coulomb field as expected. Interestingly for small separations, the eyeball fit to $\sim 1/R^4$ is quite good which may be due to a Coulomb-like behavior at small distances. (The above argument that the width must grow like R^2 does not apply because there is no string for small R.) The dielectric model [19] predicts the peak density $\sim 1/R$. Such a behavior would imply the width $\sim \sqrt{R}$ which is certainly possible in our data. We can say that the peak energy density and width are consistent with a constant value for large quark separation but we cannot rule out a slow variation. The issue can be tightened by making use of the Michael sum rules [21] as we mention in the next section.

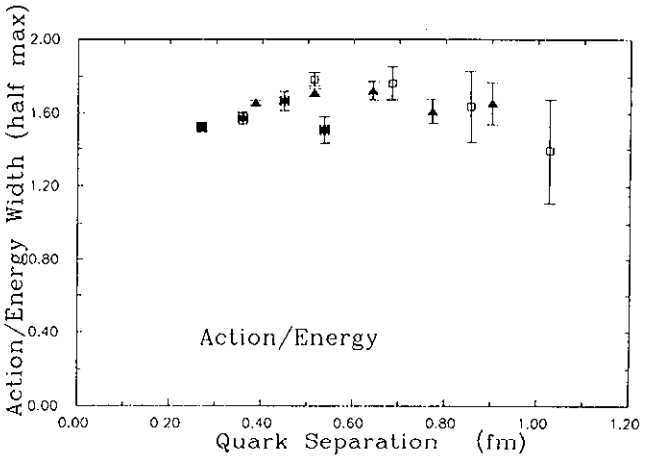

FIG. 11. Ratio of widths of action to energy profiles on center slice; labels are similar to Fig. 8.

C. Using sum rules to tighten predictions of energy behavior

A consistency check on the flux distributions can be obtained by using the Michael sum rules [21] for energy and action.

In Ref. [9] we have shown that our data are essentially consistent with these sum rules. The one difficulty is the fact that the self-energy determined from the potential differs from the self-energy determined from the action sum rule. This may be due to an ambiguity in the definition of self-energy or possibly due to our classical expressions for energy and action which ignore quantum corrections. By taking a derivative with respect to the quark separation, R, this difficulty is avoided.

Figure 10 shows the data for the ratio of the action in the center slice to the energy in the center slice, which were measured for $\beta = 2.3$, 2.4, and 2.5, at various $q\bar{q}$ separations R. One can see that for small R the ratio is small; however, at large R most data show large values (≈ 10) for the ratio, but the fluctuations at large R restrict us to a crude estimate. From the sum rules and Fig. 10 we estimate that the β function, $-(\beta \dot{a}/a) \approx 10 \pm 2$, compared to the current estimates [9,4], 7.7 ± 1.0. The asymptotic value is $-51/121 = 3\pi^2\beta/11 \approx 6.0$ for $\beta = 2.4$. There is ample evidence from other measurements that although scaling works well, asymptotic scaling is violated [25] and hence we do not expect to get the asymptotic value.

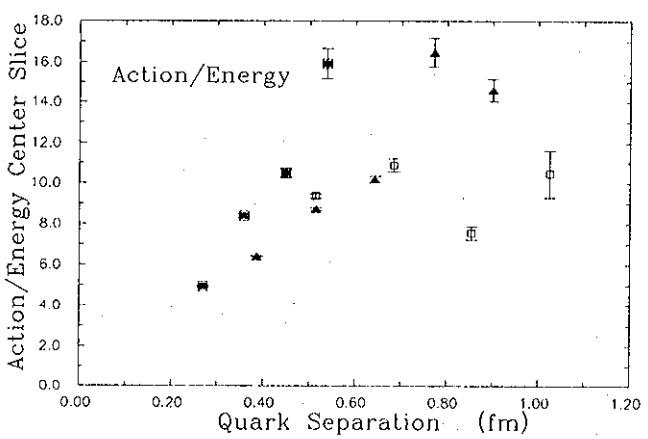

FIG. 10. Ratio of integrations of action to energy densities on center slice; labels are similar to Fig. 8.

An alternative approach is to assume the sum rules are correct and use them to infer information about the energy density from the action density, which is far easier to measure since relative errors are down by an order of magnitude. As is clear from the sum rule the action does not scale, yet the variation over these values of β is very small. An examination of Fig. 8(a) shows that the action for each β seems to stabilize to a constant for increasing distance for the peak density and for the width. This is strongly supported by data for $\beta = 2.3$ and 2.4. For $\beta = 2.5$ the quark separation R appears to be too small to draw a conclusion. From these data one can see that the peak values seem to approach a nonzero finite constant at large R. We would like to use the sum rules to predict the behavior of the energy density. A constant peak energy density follows only if the widths of the energy and action peaks have the same behavior. Figure 11 shows that in fact they do. From this and using the sum rules we conclude that the energy density stabilizes to a constant value also. This conclusion is an argument against the dielectric model [19]. However, due to the limitation on the available range of R of our data we cannot make conclusions about logarithmic behavior of the flux tube width as predicted by Lüscher [18].

D. Longitudinal profile of flux tube

To see the profile of the whole flux tube, in Fig. 12 we plot the integrations of flux action on various transverse slices along the $q\bar{q}$ axis, where $Z = 0$ is the location of one quark source, the positions of $Z < 0$ correspond to slices outside the $q\bar{q}$ pair, and the positions with $Z > 0$ correspond to slices between the $q\bar{q}$ pair. Because of the

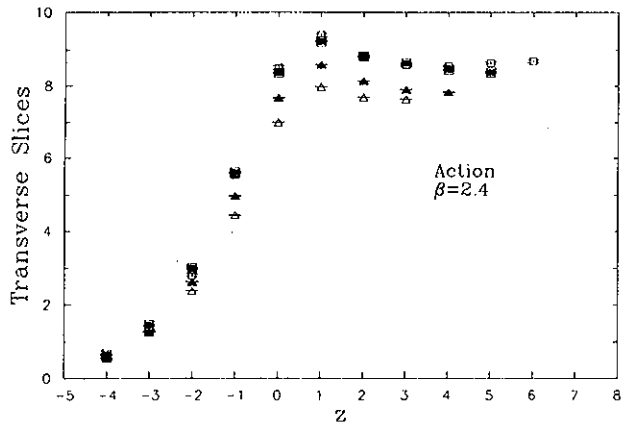

FIG. 12. Integrations of action density on transverse slices along the $q\bar{q}$ axis. The data were measured for $\beta = 2.4$ on the Wilson loops extrapolated for large time for $R = 3$ (open triangles), $R = 4$ (solid triangles), $R = 5$ (solid squares), and $R = 6$ (open squares).

symmetry of flux distribution about the midway point between the $q\bar{q}$ pair, we only show the distribution from one end to the midpoint between the $q\bar{q}$ pair. One can see that the peak values are in the neighborhood of the source, which is caused by the large self-energy concentrated around the source. However, the flux action values between the $q\bar{q}$ pair are comparable to the peak values. This implies that the integrations of flux action on the transverse slice near the $q\bar{q}$ pair are not dominated by the self-energy contributions, although the density values due to self-energy are large, their distribution regions are very narrow. This agrees with the action density distribution shown in Fig. 3(a), where the peaks of action density are restricted in a narrow region at each source. From Fig. 12 one can also see that away from the outside of the $q\bar{q}$ sources the flux action decreases rapidly with the distance from the source, and almost vanishes at the moderate distance, $R = 4a$ (i.e., $Z = -4$). However, the flux action between the $q\bar{q}$ pair is large, and is almost constant as Z increases. This agrees with the expectation for the flux tube formation.

V. SUMMARY AND CONCLUSIONS

The linear rise of the static quark potential is very well established [26]. This of course implies the existence of a flux tube. This is a critical ingredient in our understanding of confinement. In this paper, using the data generated in simulations done a few years ago, Figs. 8 and 9 indicate that we are able to reach perhaps the beginning of the flux tube plateau. The effects of the self-energies are just beginning to lose their importance at separations of about 1.0 fm. Preliminary results of this present work were reported in the conference proceedings [12].

One impediment to getting a definitive determination of the shape of the flux tube is the area law which suppresses the signal exponentially in the area of the Wilson loop. Crucial to our work was the "analytic multihit" and other techniques, described in Sec. II, to enhance the signal-to-noise. There are now well-developed techniques to "fatten" the creation and annihilation legs of the Wilson loop and greatly increase the overlap with the plaquette used to sample the energy density.

Our determination of the energy density, the lower points in Fig. 8, gives a rough value of about 3.0 ± 1.5 GeV/fm^3. However, we cannot rule out a peak density falling like $1/R$ (the higher curve at large R, arbitrarily normalized) and a width growing like $\sqrt{R}$ as predicted by Adler [19]. The second curve is the Coulomb prediction $1/R^4$ which fits the data nicely for small separations as one might expect from asymptotic freedom but has no relevance for large separations as described in Sec. IV.

A comparison between the energy and action densities suggests a way to tighten the prediction of the energy flux tube properties. Cancellations that suppress the energy by an order of magnitude are absent in the action. Although the absolute errors are the same for the two quantities, the relative errors are much smaller for the action. The surface plots in Fig. 3 show that the action density is known much more accurately than the energy density. Figure 8 shows that the peak density for the action appears to stabilize to a constant value in the range of 1.0 fm. We point out that enough information is known about the flux tube to infer from this that the energy density also stabilizes to a constant value.

The argument is based on two results. First, the Michael sum rules [23], give a fixed ratio for the integrations of the profile over the transverse plane independent of the $q\bar{q}$ separation R. Second, our most accurate measurement in the present work is the width at half maximum. Figure 11 shows that the ratio of these quantities for the action vs energy is consistent with a constant in R in the range of 0.6–1.0 fm. From these two results and the constancy of the action density we conclude that the energy density of the flux tube is also a constant independent of R.

Note added in proof. After this paper was submitted for publication, a paper by Bali *et al.* on flux tubes for SU(2) appeared [27]. This reference has significantly improved statistics over ours and reaches larger quark separations.

More recently a number of papers [28–31] pointed out that the Michael sum rules [21] are incorrect. The general feature that the action is much larger than the energy in the flux tube is still correct.

In the present paper, we rely on the fact that the sum rules predit that the ratio of the energy stored in a slice of the flux tube to the action stored in the flux tube is independent of R, the quark separation. This property is still true in the corrected sum rules.

ACKNOWLEDGMENTS

We would like to thank A. Kotanski, G. Schierholz, and T. Suzuki for many fruitful discussions on this problem. We wish to thank H. Rothe for extensive discussions on the sum rules. We thank A. Green for pointing out an important typo. R.W.H., V.S., and Y.P. were supported by the DOE under Grant No. DE-FG05-91ER40617. J.W. was supported in part by the Polish Government under Grants Nos. CPBP 01.01 and CPBP 01.09.

[1] M. Fukugita and T. Niuya, Phys. Lett. **132B**, 374 (1983).
[2] J. W. Flower and S. W. Otto, Phys. Lett. **160B**, 128 (1985).
[3] R. Sommer, Nucl. Phys. **B291**, 673 (1987).
[4] R. Sommer, Nucl. Phys. **B306**, 180 (1988).
[5] J. Wosiek and R. Haymaker, Phys. Rev. D **36**, 3297 (1987); J. Wosiek, in *Field Theory on the Lattice*, Proceedings of the International Conference, Seillac, France, 1987, edited by A. Billoire *et al.* [Nucl. Phys. B (Proc. Suppl.) **4**, 52 (1988)].
[6] R. W. Haymaker and J. Wosiek, Acta Phys. Pol. B **21**, 403 (1990).
[7] R. W. Haymaker, Y. Peng, V. Singh, and J. Wosiek, in *Lattice '89*, Proceedings of the International Symposium, Capri, Italy, edited by R. Petronzio *et al.* [Nucl. Phys. B (Proc. Suppl.) **17**, 558 (1990)].
[8] R. W. Haymaker, Y. Peng, V. Singh, and J. Wosiek, in *The Rice Meeting*, Meeting of the Division of Particles and Fields of the APS, Houston, Texas, edited by B. Bonner and H. Miettinen (World Scientific, Singapore, 1990).
[9] R. W. Haymaker and J. Wosiek, Phys. Rev. D **43**, 2676 (1991).
[10] R. W. Haymaker, V. Singh, and J. Wosiek, in *Lattice '90*, Proceedings of the International Symposium, Tallahassee, Florida, edited by U. M. Heller, A. D. Kennedy, and S. Sanielevici [Nucl. Phys. B (Proc. Suppl). **20**, 207 (1991)].
[11] T. Barczyk, R. W. Haymaker, V. Singh, E. Laermann, and J. Wosiek, in *Lattice '91*, Proceedings of the International Symposium, Tsukuba, Japan, edited by M. Fukugita *et al.* [Nucl. Phys. B (Proc. Suppl.) **26**, 462 (1992)].
[12] R. W. Haymaker, V. Singh, D. Browne, and J. Wosiek, in *Proceedings of the Workshop on QCD Vacuum Structure and its Applications*, Paris, France, 1992, (World Scientific, Singapore, 1993), p. 184.
[13] G. Parisi, R. Petronzio, and F. Rapuano, Phys. Lett. **128B**, 418 (1983).
[14] H. D. Trottier and R. M. Woloshyn, Phys. Rev. **48**, 2290 (1993).
[15] E. Marinari, in *Lattice '88*, Proceedings of the International Symposium, Batavia, Illinois, edited by A. S. Kronfeld and P. B. Mackenzie [Nucl. Phys. B (Proc. Suppl.) **9**, 209 (1989)].
[16] G. S. Bali, C. Schlichter, and K. Schilling, in *Lattice '93*, Proceedings of the International Symposium, Dallas, Texas, edited by T. Draper *et al.* [Nucl. Phys. B (Proc. Suppl.) **34**, 216 (1994)].
[17] M. Lüscher, Nucl. Phys. **B180** [FS2], 317 (1981).
[18] M. Lüscher, G. Münster, and P. Weisz, Nucl. Phys. **B180** [FS2], 1 (1981).
[19] S. L. Adler, Nucl. Phys. **B217**, 381 (1983).
[20] M. Baker, J. S. Ball, and F. Zachariasen, Phys. Rev. D **41**, 2612 (1990).
[21] C. Michael, Nucl. Phys. **B280** [FS18], 13 (1987).
[22] R. D. Mawhinney, Phys. Rev. D **41**, 3209 (1990).
[23] B. Bunk (unpublished).
[24] M. David, *Geostatistical Ore Reserve Estimation* (Elsevier, New York, 1977).
[25] C. Michael, Phys. Lett. B **283**, 103 (1992).
[26] S. P. Booth *et al.*, Phys. Lett. B **275**, 424 (1992).
[27] G. S. Bali, C. Schlichter, and K. Schilling, Phys. Rev. D **51**, 5165 (1995).
[28] H. G. Dosch, O. Nachtmann, and M. Reuter, Heidelberg Report No. HD-THEP-95-12, hep-ph 9503386 (unpublished).
[29] H. Rothe, Phys. Lett. B **355**, 260 (1995).
[30] H. Rothe, Heidelberg Report No. HD-Thep-95-35, heplat 9508005 (unpublished).
[31] C. Michael, Liverpool Report No. LTH 348, heplat 9504016 (unpublished).